COMPUTATIONAL ANALYSIS OF HIGH REYNOLDS NUMBER AERO-STRUCTURAL DYNAMICS (HIRENASD) EXPERIMENTS

Lars Reimer[1], Alexander Boucke[2], Josef Ballmann[3], and Marek Behr[4]

[1]LFM/CATS, RWTH Aachen University
Schinkelstr. 2, 52062 Aachen, Germany
reimer@cats.rwth-aachen.de

[2]ITAM Consulting
Oberforstbacher Str. 230, 52076 Aachen, Germany
boucke@itam-gmbh.de

[3]LFM, RWTH Aachen University and ITAM Consulting
Schinkelstr. 2, 52062 Aachen, Germany
ballmann@lufmech.rwth-aachen.de

[4]CATS, CCES, RWTH Aachen University
Schinkelstr. 2, 52062 Aachen, Germany
behr@cats.rwth-aachen.de

Keywords. Aero-Structural Dynamics, Steady/Unsteady Computational Aeroelasticity, Reduced-Order Structural Modelling, High Reynolds Number Flows

Abstract. This paper presents comparisons between RANS-based time-domain aero-structural dynamics (ASD) simulations and selected results from the HIRENASD (*Hi*gh *Re*ynolds *N*umber *A*ero-*S*tructural *D*ynamics) wind tunnel experiments. At first the experimental setup and the applied computational ASD (CASD) solver are briefly presented. Changes of lift, pressure distribution and wing bending deflection measured during steady polars at different parameter combinations of Mach number and model loading factor are compared to results from numerical simulations. The influences of different turbulence models on the agreement between measured and computed lift-over-drag polars is assessed thereafter. A revision of the structural identification of the numerical model is discussed which reveals a significant influence of the model support on eigenshapes and eigenfrequencies. The unsteady pressure fluctuations and model accelerations which were computed for three separately excited wing modes (both first flap-bending dominated and first torsion dominated modes) are compared to the corresponding experimental results. Thereby the capability of the employed CASD solver to accurately quantify experimentally observed relations between harmonic structural motion and transonic aerodynamics is demonstrated. This bodes well for upcoming comparisons of simulations and dynamic HIRENASD experiments.

1 INTRODUCTION

Dynamic aeroelastic experiments conducted in the transonic flow regime at high Reynolds numbers are still scarce and results are often not accessible. However, measured data is necessary for a better understanding of transonic aeroelastic phenomena. Also, it is required for the validation of today's advanced CASD methods which are to overcome the limitations of commonly employed frequency domain analysis methods. Against this backdrop the HIRENASD project was initiated within the Collaborative Research Centre SFB

401 [1] at RWTH Aachen University with funding by the German Research Foundation (DFG) in 2004. High Reynolds number ASD experiments were successfully conducted with an elastic supercritical wing in November 2006 in the European Transonic Windtunnel (ETW). The aeroelastic behaviour of the wing model was studied during steady polars at slowly varying angle of attack and during dynamic aeroelastic tests at fixed root angle of attack under vibration excitation in the wing root region. These experiments were performed at different Mach numbers, Reynolds numbers and model loading factors q/E (ratio of dynamic pressure and Young's modulus). Prior to the HIRENASD wind tunnel test campaign the authors of this paper supported the preparation of the experiments by numerically predicting the aeroelastic wing behaviour for nearly all projected wind tunnel conditions [2] employing the in-house CASD code SOFIA and thus assuring the viability of the wind tunnel model.

Since measured data from all steady HIRENASD experiments and from almost all dynamic experiments have been evaluated, this paper reports about the validation of the SOFIA code against selected evaluated data. To be more precise, SOFIA is assessed regarding its capability to predict aeroelastic equilibrium configurations of static polars for two out of three independent parameter variations studied during the HIRENASD experiments, these being Mach number and loading factor q/E. Because the accurate prediction of shock-induced separation and its interaction with the model deformation are crucial at high transonic Mach numbers and high angle of attacks, different turbulence models were employed and their effects on static polars investigated. The influence of harmonic excitation of different mode shapes of the HIRENASD wing model on the amplitudes of the surrounding pressure distribution relative to excited model accelerations is studied numerically and the results are compared with experimental observations. These revealed that the correct representation of experimental mode shapes in the numerical model of the HIRENASD setup is very sensitive to the correct structural identification of the model support. Consequently, the structural identification of the model was revised and resulting effects are discussed here.

2 THE HIRENASD WIND TUNNEL MODEL

The HIRENASD wing model corresponds to the SFB 401 clean wing reference configuration with a planview typical for wings of high speed transport aircrafts [1]. It is a wing model with a semispan of almost 1.30m, an aerodynamic mean chord of 0.3445m, a constant leading edge sweep of 34° and a trailing edge with two kinks, segmenting the wing into three spanwise sections. The aerodynamic profile of the wing is defined according to the supercritical BAC 3-11/RES/30/21. The relative thickness in the innermost section I changes spanwise conically from 15% to 11%, whereas in both outer sections the relative thickness remains constant at 11% (to the right of Fig. 1). To permit good access to the internal instrumentation, the wing is composed of two bolted shells made of Vascomax C-200. This special steel is optimised for use under cryogenic conditions. Its Young's modulus exhibits a temperature dependence given as E=190.3GPa $-$ 0.0416GPa/K$(T-77\text{K})$.

The model was arranged hanging from the wind tunnel ceiling into the test section of ETW. To reduce the influence of the boundary layer developing along the ceiling, a fuselage substitute was designed. It is fixed on the wind tunnel turntable without having any mechanical contact with the wing and being designed very stiff. The aerodynamically relevant part of the HIRENASD model is depicted in the left part of Fig. 1 as is placed

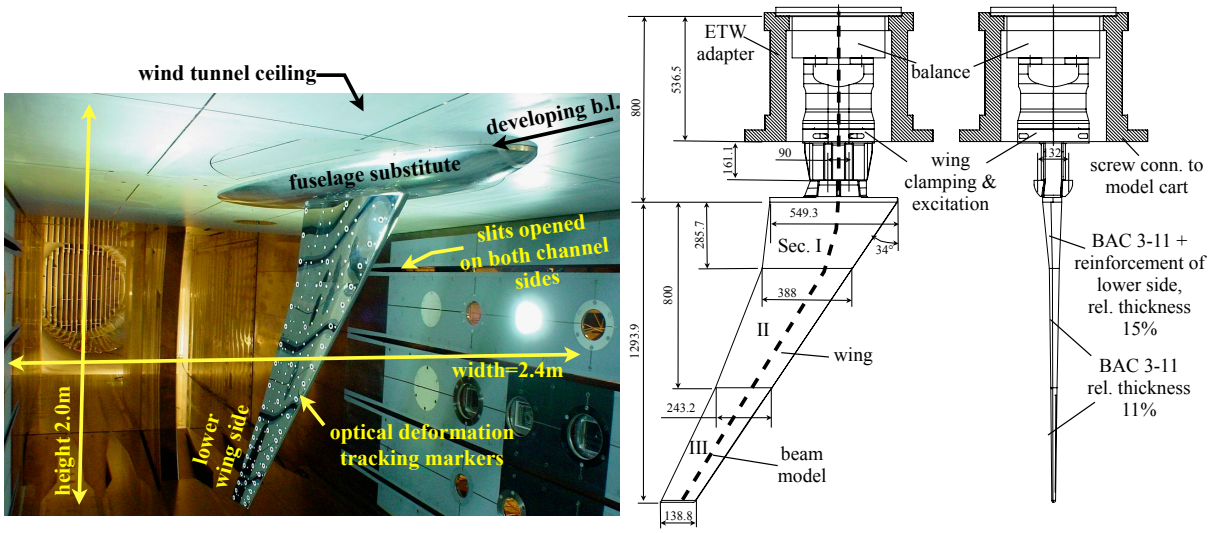

Figure 1: HIRENASD wing model in ETW test section and basic geometric dimensions of the full wind tunnel model assembly including the connection device to ETW's model cart. Note: The beam axis of the housing of the excitation mechanism and the connection device to ETW's model cart coincide visually with the beam axis of the wing balance, although each part is identified as a separate beam here

in ETW's test section.

The supporting part of the HIRENASD model, which is located above the wind tunnel ceiling, is designed as follows: The wing model is mounted on a piezo-electrical 6-components balance which is specifically tailored to the needs of dynamic force recording during HIRENASD experiments [3]. The full assembly is connected to ETW's model cart with a cylindrical adapter and thereby prepared to be placed in the measuring section of ETW as for half-model testing. To enable dynamic aeroelastic experiments, force couples acting in spanwise direction can be applied to the wing root plane by a vibrational excitation mechanism which is housed inside the wing clamping device. The latter is connected to the balance by a cylindrical shell.

Besides its instrumentation with accelerometers and strain gauges, the wing model is equipped with a large number of in-situ pressure sensors located in seven spanwise sections for high-precision dynamic pressure measurement. A 3D surface pattern tracking (SPT) system was employed to measure optically the deformations of the wing during the tests. Further details regarding the experimental setup and instrumentation are given in [3–6].

3 THE APPLIED AERO-STRUCTURAL DYNAMICS SOLVER

The ASD solver SOFIA applied here follows a partitioned approach, in which separate programs are operated iteratively for the solution of structural deformation and the flow solution on a deforming grid. A modular interface structure is provided by the in-house Aeroelastic Coupling Module (ACM) [7], allowing different flow and structural solvers to be integrated without great programming effort. As is described below more in detail, the flow solver FLOWer was coupled to the structural dynamics solver FEAFA via the ACM in this paper. Then the latter controlled the sequence of solver calls and the transfer of aerodynamic loads and structural deformations in mutual directions between flow field and structural partition.

The load and deformation transfer between wetted surface and structure is carried out with Finite Interpolation Elements [8], which are well-suited for non-matching grid interfaces. The algorithm which is implemented in the ACM can be summarised as follows: At first each surface grid point is projected separately onto the next finite element of the structural mesh. A rigid connection between the surface grid point and its projection point is assumed. The interpolation between projection point and nodes of the structural mesh are performed by using the shape functions of the respective finite element to which the project point belongs. To ensure smoothness between intersecting surface parts of multi-component configurations, blending techniques are introduced into this transfer scheme [7, 9]. The resulting overall procedure is a robust and computationally very efficient scheme, since only algebraic expressions have to be evaluated.

In this paper steady aeroelastic computations are performed in the sense of an under-relaxed block Gauss-Seidel scheme, meaning one field is iterated after exchanging the coupling data while the other is held constant. A reasonable choice of the relaxation parameter provided, the aeroelastic equilibrium configuration (AEC) could generally be reached after no more than 7 coupling iterations between flow solver and structural solver. 0.7 has proven to be a good value for the relaxation parameter. In each coupling step the flow solver converged sufficiently in 150 multigrid iterations until the next deformation state of the aerodynamic surface is computed by the structural solver.

Unsteady aeroelastic simulations conducted in this paper (see sec. 6) were advanced in time by applying loose temporal aeroelastic coupling. This was controlled by the ACM in the manner of the following predictor-corrector scheme: For the predictor step the projected aerodynamic loads are extrapolated to the next time step with 2^{nd} order accuracy. With this extrapolated right hand side vector of the structural dynamics equations, displacement, velocity and acceleration is determined for the next time step. Then CFD grid deformation is carried out based on the deformed surface that arises from projecting the structural deformation onto the CFD surface mesh. Now the flow simulation can be performed for the next time step. In the final corrector step the structural solution for the next time step is repeated with the computed loads instead of the extrapolated ones. This scheme is preferred here due to its lower computational cost over a tight coupling scheme which is however provided by the ACM.

The representation of the wing model structure by multi-axial Timoshenko beam elements is favoured here since these offer an accurate displacement computation for slender structures at low computational cost. The discretisation of the HIRENASD model by a beam idealisation is shown in Fig. 1 on the right. An implementation of the multi-axial Timoshenko beam element [7, 10] is available in the in-house code *F*inite *E*lement *A*nalysis *f*or *A*eroelasticity (FEAFA) apart from higher-dimensional element types as are available in commercial FE packages. In the unsteady cases, the time integration of the structural dynamics equations was carried out in modal coordinates, with 12 modes being considered. This number is a compromise. On the one hand it is sufficiently large to allow an accurate computation of the deformation state. On the other hand the time step, which must hold the Shannon theorem for all considered eigenfrequencies, is large enough to advance the solution in physical time in reasonable computational time. The integration of the uncoupled modal equations was perfomed by applying Newmark's method with subcycling such that the periods of all considered modes were resolved by 800 time steps.

All results presented in this paper were obtained using the FLOWer code as the flow solver which has been developed under the leadership of the German Aerospace Centre (DLR) during the projects MEGAFLOW I/II [11]. It solves the 3D time-dependent Reynolds-averaged Navier-Stokes (RANS) equations for perfect gases on deformable multi-block structured grids and offers algebraic turbulence models, various eddy-viscosity-based turbulence models and Reynolds stress models. In all unsteady simulations dual-time stepping was used in the flow solver with a minimum of 15 and a maximum of 75 iterations in pseudo time per physical time step. Generally, the pseudo-time iterations could be aborted after 25 steps because the density residual threshold of 10^{-5} was reached. The flow solver operated with second order accuracy in space and time with an additional first order extrapolation of conservative variables in time.

For the deformation of multiblock-structured grids (e.g. FLOWer grids) the in-house code *Mu*ltiblock *Gri*d *D*eformation T*o*ol (MUGRIDO) [10, 12] was applied. It generates a fictitious framework of beams by modelling the CFD block boundaries and a given percentage of grid lines as massless linear elastic Timoshenko beams. These are assembled to a beam framework which is then deformed based on the motion of those elements which lie on the aerodynamic surface. A well shaped volume CFD grid is efficiently reconstructed from the deformed beam framework by 2D- and 3D-interpolation.

4 NUMERICALLY PREDICTED AEROELASTIC EQUILIBRIUM CONFIGURATIONS COMPARED TO EXPERIMENTS

In this section, the agreement between static experimental polars and respective aeroelastic computations is studied and compared to results of simulations that disregard model deformation. The focus lies on HIRENASD test series Nos. 5 and 6 here. In both series the Reynolds number is $23.5 \cdot 10^6$. The Mach number varies between 0.70 and 0.88. The level of q/E is only $0.22 \cdot 10^{-6}$ in series 6, whereas it is more than doubled to $0.48 \cdot 10^{-6}$ in series 5. The quantities which are used to compare simulation and experiment are lift and drag coefficients of the wing, pressure distributions at 7 spanwise sections and the wing bending displacement which was recorded by the SPT device. While influence from Ma number, angle of attack and loading factor q/E are investigated, the impact of systematic variations of Reynolds number on the AEC is not treated here, although it was done in the experiments.

The steady aeroelastic results discussed in this section were obtained before the revision of the structural model was made. Hence, the structural model which is assigned as model A in section 5 was used for obtaining the results in this paper. This model does not include the influence arising from the flexibility of the connection between ETW adapter and balance. The reduction of load-bearing capacities in the model support region which features strong changes of geometrical dimensions was also not considered in model A correctly. But all aforementioned modifications which are included in model C affect primarily the dynamic aeroelastic model behaviour. Therefore all results presented in this section would be obtained most likely for the revised model C as well.

Based on the temperature of the incoming flow which is between T_∞=99K (exp. 319, series 6: Ma=0.88, q/E=$0.22 \cdot 10^{-6}$) and T_∞=199K (exp. 248, series 5: Ma=0.70, q/E=$0.48 \cdot 10^{-6}$) the material properties of the beam model discretising the wing were set in accordance to their temperature dependence (see section 2). The material proper-

ties for balance and excitation were set to those at ambient conditions in all simulations (T_{tot}=297K) since the assembly parts above the turn-table are thermally insulated from the cold flow.

In the preparatory simulations prior to the HIRENASD test campaign, the fuselage substitute and boundary layer at the wind tunnel ceiling were not considered to reduce the computational problem size. But for comparison with experimental data which is targeted here the consideration of both influences evinced to be necessary [2, 7]. Therefore the surface of the wing model and fuselage substitute are both exposed to the flow in the RANS-based flow grid applied here. Additionally the boundary layer developing at the wind tunnel ceiling is captured by imposing a no-slip condition at the respective domain boundary. This leads to a boundary layer thickness of about 6.5cm at Re=$23.5 \cdot 10^6$ due to an assumed development length of the boundary layer of 9m infront of the model. Farfield conditions were imposed on all remaining domain boundaries far away from the model as advised by ETW because the side wall slits were opened during all HIRENASD tests (see Fig. 1, left).

Simulations were carried out almost exclusively using LEA k-ω turbulence model assuming fully turbulent flow which is reasonable at Reynolds numbers above 20 million. At test conditions below Re=$23.5 \cdot 10^6$ laminar-turbulent transition was forced by a tripping device which was attached close to the leading edge. To study the influence on the AEC that arises from the choice of the turbulence model, additional simulations were performed with the Spalart-Allmaras one-equation model and the SSG-ω Reynolds stress model (see sec. 4.3).

4.1 Aeroelastic Behaviour of the Global Lift Coefficient

Since backward-swept wings experience a spanwise reduction of local angles of attack when being bent upwards, their integral lift coefficient is always lower than for a wing without any deformation. This behaviour becomes also apparent for the HIRENASD wing in Figs. 2 and 3. Both figures display the change of global lift coefficient with increasing angle of attack at wing root for Mach numbers 0.75, 0.80 and 0.85. The lift loss with respect to simulations disregarding wing deformation (blue dashed curves) is higher in Fig. 3 because the wing loading factor q/E=$0.48 \cdot 10^{-6}$ is more than double the value of series 6 (q/E=$0.22 \cdot 10^{-6}$) shown in Fig. 2. For Mach numbers 0.75 and 0.80 the improvement with respect to experimental results by considering model deformation is significant. Here the agreement between aeroelastic simulation and experiment is almost perfect for both levels of q/E. The streamline patterns displayed in combination with c_p distributions about AECs at different Mach numbers for α=5° and −2° enable insights how the wing deformation interacts with the flow separation. While the flow is already separated for the complete outer wing sections at Ma=0.75 for the lower level of q/E, it is still completely attached for q/E=$0.48 \cdot 10^{-6}$. For Ma=0.80 the flow is detached for the two outer wing sections if a rigid wing is assumed. The flow reattaches again in the outermost wing section if the aerodynamic twist is correctly captured. For Ma=0.85 and at higher angles of attack nonlinearity becomes prominent in c_L-α curves. Then the flow separates over almost the complete upper side of the wing after three quarters of local chord. This challenging flow situation may cause the deviations in lift which arise between simulation and experiment for Ma=0.85.

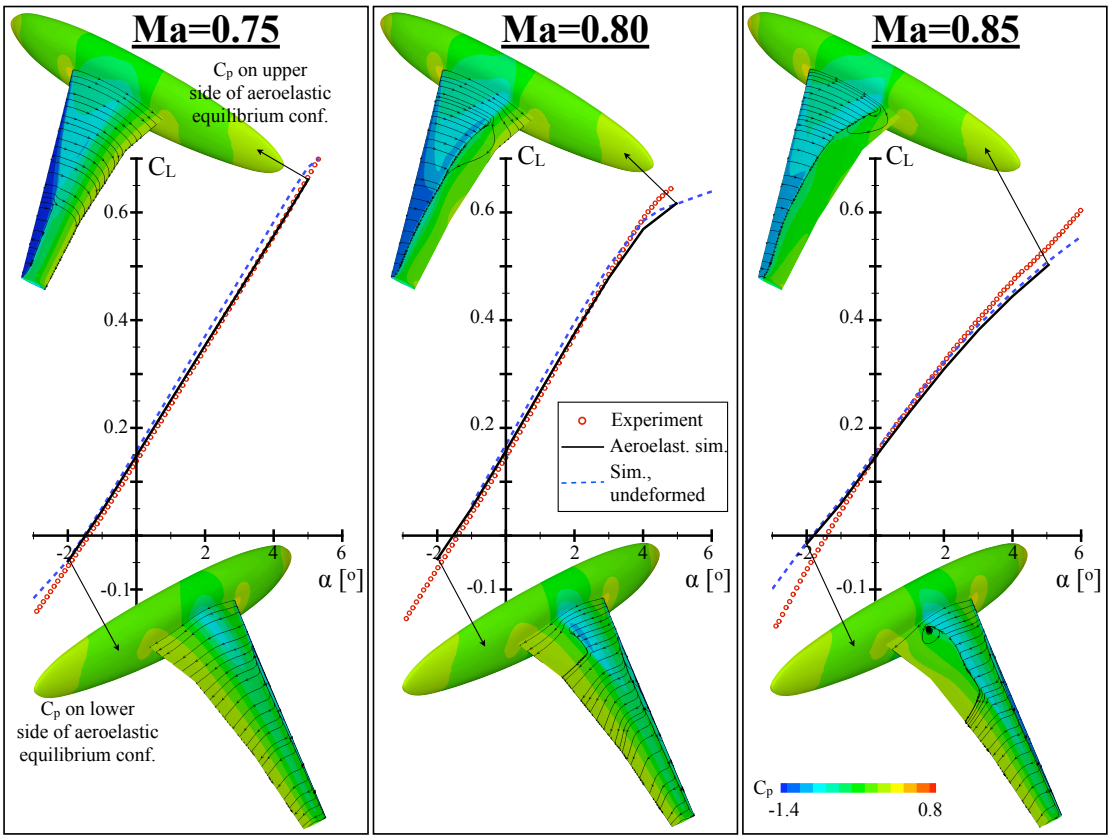

Figure 2: Changes of lift coefficient with angle of attack in the experiments of series 6 (Ma=0.75 (exp. 315), Ma=0.80 (exp. 316), Ma=0.85 (exp. 318), Re=$23.5 \cdot 10^6$, $\mathbf{q/E{=}0.22 \cdot 10^{-6}}$) compared to those predicted by aeroelastic simulations and for an undeformed configuration

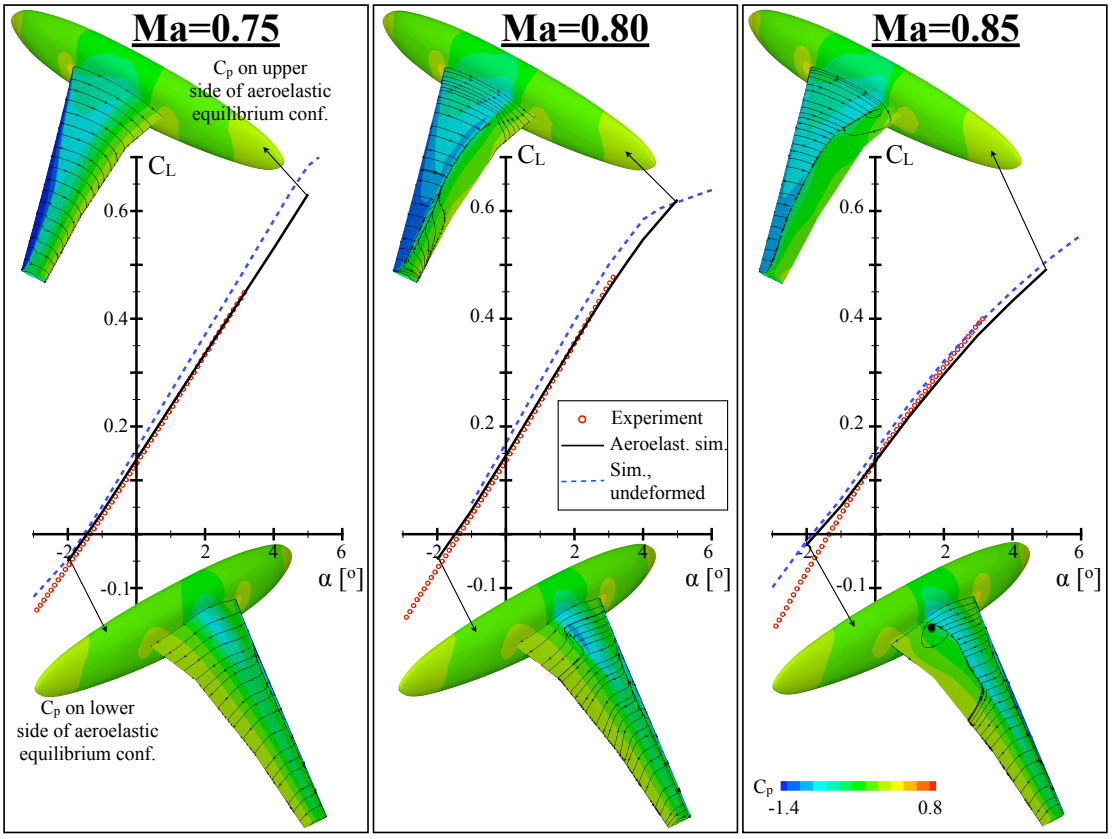

Figure 3: Changes of lift coefficient with angle of attack in the experiments of series 5 (Ma=0.75, (exp. 249), Ma=0.80 (exp. 250), Ma=0.85 (exp. 252), Re=$23.5 \cdot 10^6$, $\mathbf{q/E{=}0.48 \cdot 10^{-6}}$) compared to those predicted by aeroelastic simulations and for an undeformed configuration

Because zero lift is about α=−1.3° for the wing, the impact of wing deformation on streamline patterns and c_p distribution is hardly visible at α=−2°. At this angle of attack it is difficult to obtain a converged coupled solution. This is due to a strong shock occuring where the airfoil is thickened from originally 11% to 15% relative thickness in the inner section on the lower wing side. In addition, a separation region is present at negative α shortly behind the characteristic turning point in the nose region of the BAC-3/11 airfoil on the lower side, even for low Mach numbers. This behaviour may account for the differences between experiment and simulation for negative α.

4.2 Change of Spanwise Pressure Distribution with Increasing Mach Number

The divergence of the integral lift coefficient with increasing Mach number which is apparent from the reduced inclination of the c_L-α curves between Figs. 2 and 3 is even more prominent in the upper left diagram of Fig. 4. The divergent behaviour of the curves is well captured by aeroelastic simulations in terms of the lift slope and the Mach number at divergence onset. Although the absolute lift value is predicted less accurately with increasing angle of attack, the Mach number from which the curves diverge is determined correctly for all angles of attack, even for α=5°. For this case the pressure distributions at Ma=0.75, 0.80, 0.83, 0.85, and 0.88 (Re=$23.5 \cdot 10^6$, q/E=$0.22 \cdot 10^{-6}$) are compared between simulation and experiment in the 7 spanwise sections which were equipped with pressure sensors. Fig. 4 reveals that flow separation increasingly dominates the wing with rising Mach number. Overall we obtain a very good agreement between simulation and experiment. Almost all shock positions, suction peaks and general pressure behaviours along local chords are predicted in very good agreement with the experiments. Slight deviations are present in the pressure level after shock induced separations in the outer sections and in particular in both inner sections for $Ma > 0.80$ where the computed shock position is slightly more upstream than in the experiment.

4.3 Influence of Turbulence Modelling on Aeroelastic Lift-over-Drag Polars

The results presented so far were exclusively achieved with the LEA k-ω two-equation turbulence model. Deviations between experiment and simulation were observed which might be connected to the way the flow separation is predicted. The influence of different turbulence models on the flow pattern and integral aerodynamic coefficients was investigated by utilizing the Spalart-Allmaras (SA) one-equation model and the SSG-ω Reynolds stress model (RSM) instead of the LEA model. Although the RSM appears to compute the best approximation for lift-over-drag polars, the lift coefficients alone are way to high compared to the experiment. This is caused by higher resulting suction levels and by shock onsets which are substantially more downstream than computed by all one- and two-equation eddy-viscosity models. The SA model leads to a stronger flow separation in the inner wing section than is computed by the LEA model. The shock position it produces in the middle wing section is more upstream. Thereby integral lift coefficients are slightly lower for the SA than for the LEA model. With respect to drag coefficients, simulations employing the SA model show values which are considerably higher than in the experiments, in particular at Ma=0.80. Because at high Mach numbers the flow detaches over almost the entire wing anyhow, SA's inherent tendency to produce stronger separations is not as crucial as at lower Mach numbers. Therefore the agreement between the drag polars computed with the SA model and the experimental results actually improves with increasing Mach number.

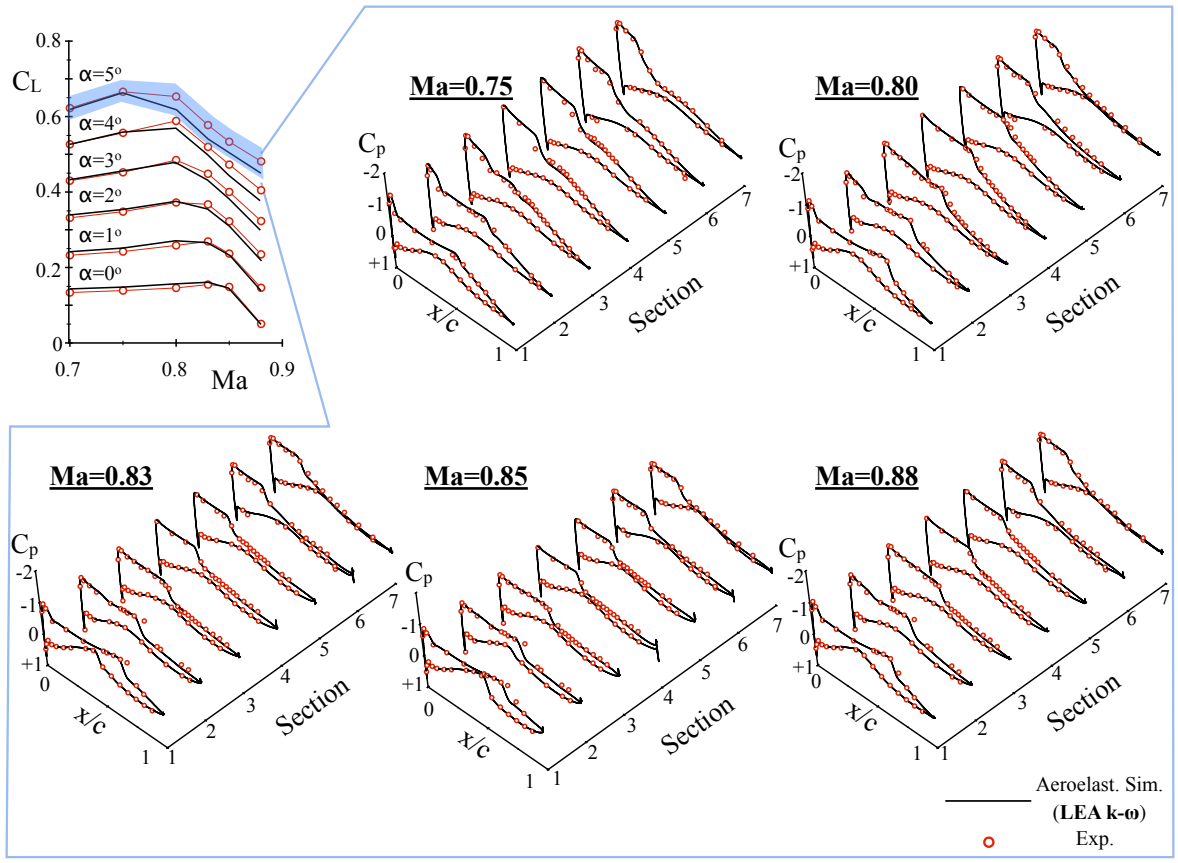

Figure 4: Divergence behaviour of global lift coefficient with increasing Mach number and the corresponding changes of c_p distributions in spanwise pressure measuring sections (series 6 (exp. 314-318): Ma=0.70-0.88, Re=$23.5 \cdot 10^{-6}$, q/E=$0.22 \cdot 10^{-6}$)

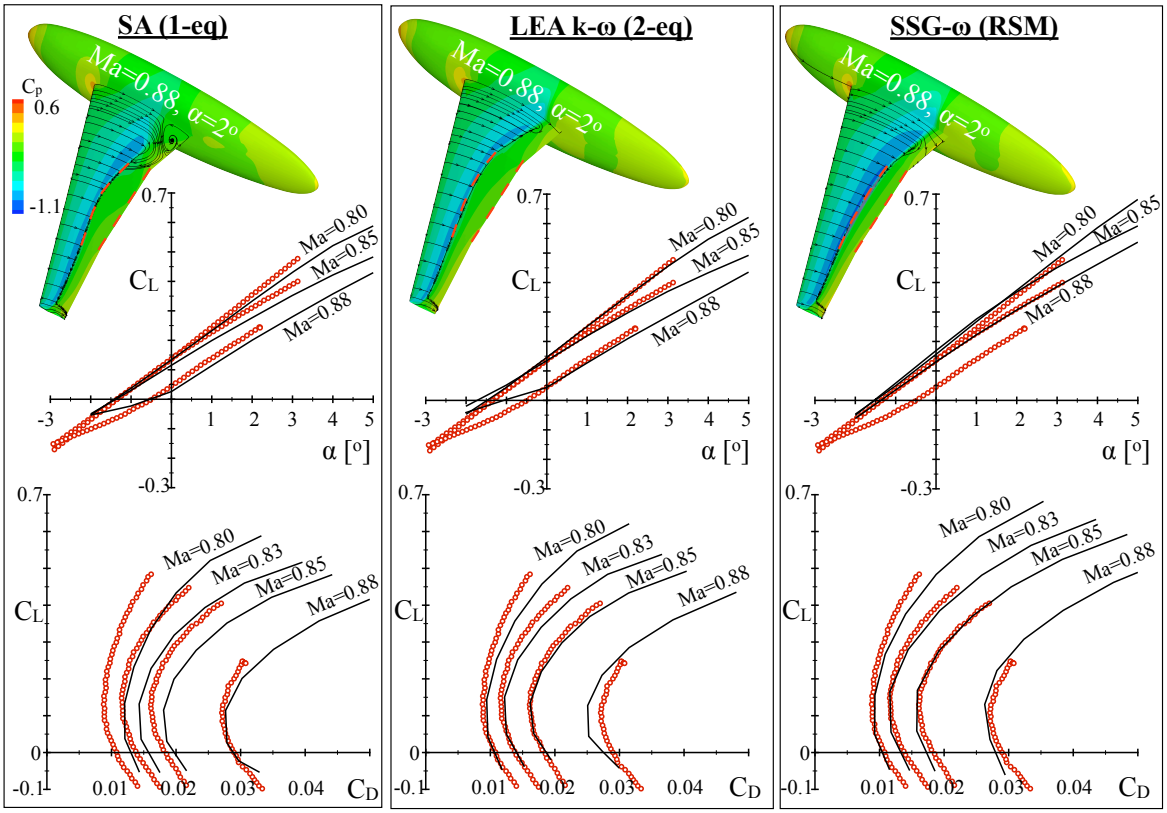

Figure 5: Influence of the turbulence model (from left to right: Spalart Allmaras, LEA k-ω and Reynolds stress model SSG-ω) on lift and lift-over-drag curves (series 5 (exp. 250-253): Ma=0.80-0.88, Re=$23.5 \cdot 10^{-6}$, q/E=$0.48 \cdot 10^{-6}$)

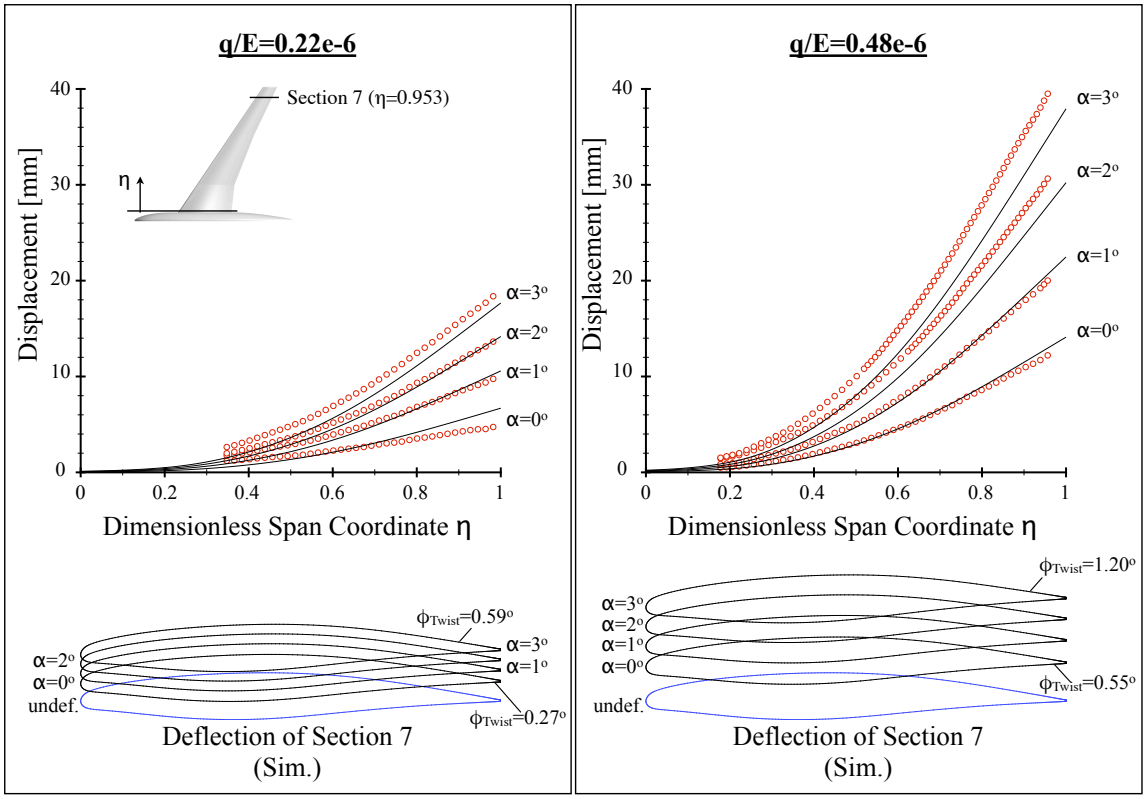

Figure 6: Comparison of the spanwise wing deformation between experiment and simulation for two different loading factors q/E=$0.22 \cdot 10^{-6}$ and $0.48 \cdot 10^{-6}$ (here for exp. 316 (series 6) and 250 (series 5), both conducted at Ma=0.80, Re=$23.5 \cdot 10^6$)

4.4 Change of Spanwise Model Deformation with Increasing Loading Factor

Apart from the Mach number, the stagnation pressure q, or more precisely the ratio of q and the Young's modulus of the model material at wind tunnel temperature, is the most significant factor influencing the AEC. q/E scales the model deformation almost linearly, as can be seen in Fig. 6. The bending deformation of the wing is plotted against the non-dimensional spanwise coordinate η for q/E=$0.22 \cdot 10^{-6}$ and $0.48 \cdot 10^{-6}$ and four different angles of attack at Ma=0.80 and Re=$23.5 \cdot 10^6$. The experimental data displayed in Fig. 6 was evaluated from marker displacements that were recorded by the SPT system used in the HIRENASD tests at the same q/E levels as in the simulations, but at different Reynolds numbers (Re=$7 \cdot 10^6$ at q/E=$0.22 \cdot 10^{-6}$ and Re=$14 \cdot 10^6$ at q/E=$0.48 \cdot 10^{-6}$). The deviations between model deformation in experiments and simulations can not be attributed to differing Reynolds numbers here, since the Re effect on model deformation is of minor importance compared to the effect of q/E. For the lower level of q/E the difference at 90% span reaches its maximum of about 8.5%. This increases to 12.3% for the higher q/E level. While the shape of the bending curve and its change with angle of attack are in acceptable agreement with the experiments, most of the deviations appear to result from the inner wing section.

5 REVISION OF DYNAMIC PROPERTIES OF THE NUMERICAL STRUCTURAL MODEL

Deviations between the dynamic properties of the Timoshenko beam model used so far for the numerical model of the HIRENASD wind tunnel assembly [2, 7] and those identified by laboratory tests [3] and in excitation tests in ETW at wind-off conditions [6] motivated a revision of the beam identification. Possible effects arising from the manner of composing the wing model from two shells were not part of this investigation. The numerical modelling for the wing still assumes that both shells are perfectly joint together and full force closure exists between both shells. While the Timoshenko beam modelling for the wing was already compared in-depth to a generated tetrahedral volume model [7], a comparable analysis for the mounting of the HIRENASD model was still lacking. In contrast to the wing geometry, this part exhibits some rapid changes of geometric dimensions, in particular the transition region between wing and excitation mechanism and the connection between upper and lower part of the balance via pre-stressed bolts and piezo-sensors. In these regions the stiffnesses derived directly from geometric dimensions of the respective cross-sections differ considerably from the actual stiffnesses due to reductions of the load-bearing cross-sectional areas. This had not been considered in the beam modelling so far.

In Fig. 7 the mode shapes and vacuum eigenfrequencies of the existing beam modelling of the wing are opposed to the corresponding ones of a tetrahedral volume model. To ease the comparison between both models, the mode shapes of the Timoshenko beam model were projected onto the volume mesh. The figure visualises the first four flap-bending dominated modes and the first torsion dominated mode. The contour colouring represents the displacement magnitudes of the respective mass-normalised eigenvectors. The volume model is converged in the sense of spacial grid resolution. It has a maximum element size of 9mm and consists of 123000 quadratic tetrahedron elements (Tet10). In contrast, about 200 Timoshenko beam elements are sufficient to show the results in Fig. 7. The clamping of the wing applied here imitates the way the excitation mechanism is mounted to the wing in reality (cf. the right part of Fig. 1 with Fig. 7). The eigenfrequencies of the flap-bending dominated modes of the beam model are slightly higher compared to those of the volume model, but the maximum difference remains below 2.1% for the highest mode shown here. Because the beam modelling employed here disregards warping restraints, the torsional eigenfrequency of the volume model is about 0.8% higher. It is to be emphasised here that both models enable a unique identification of the dominant modal deformation as either a flap-bending or torsion dominated mode. The lag-bending dominated mode is not considered at all here because of its minor importance for the aeroelastic model behaviour.

The revision of the stiffness distribution of the beam model, which also represents the excitation mechanism and the balance (model B), against a proper volume model resulted in reductions of all eigenfrequencies compared to the previous beam (model A) as is shown in Fig. 8. Even though the revised beam (model B) still exhibits higher eigenfrequencies for the flap-bending dominated modes resp. a lower one for the torsion dominated mode than the volume model, the difference between the eigenfrequencies of both models could be reduced substantially. The most prominent influences on reductions of eigenfrequencies arise from the transition region between wing clamping and excitation mechanism as well as from the connection region between upper and lower balance parts. The influences

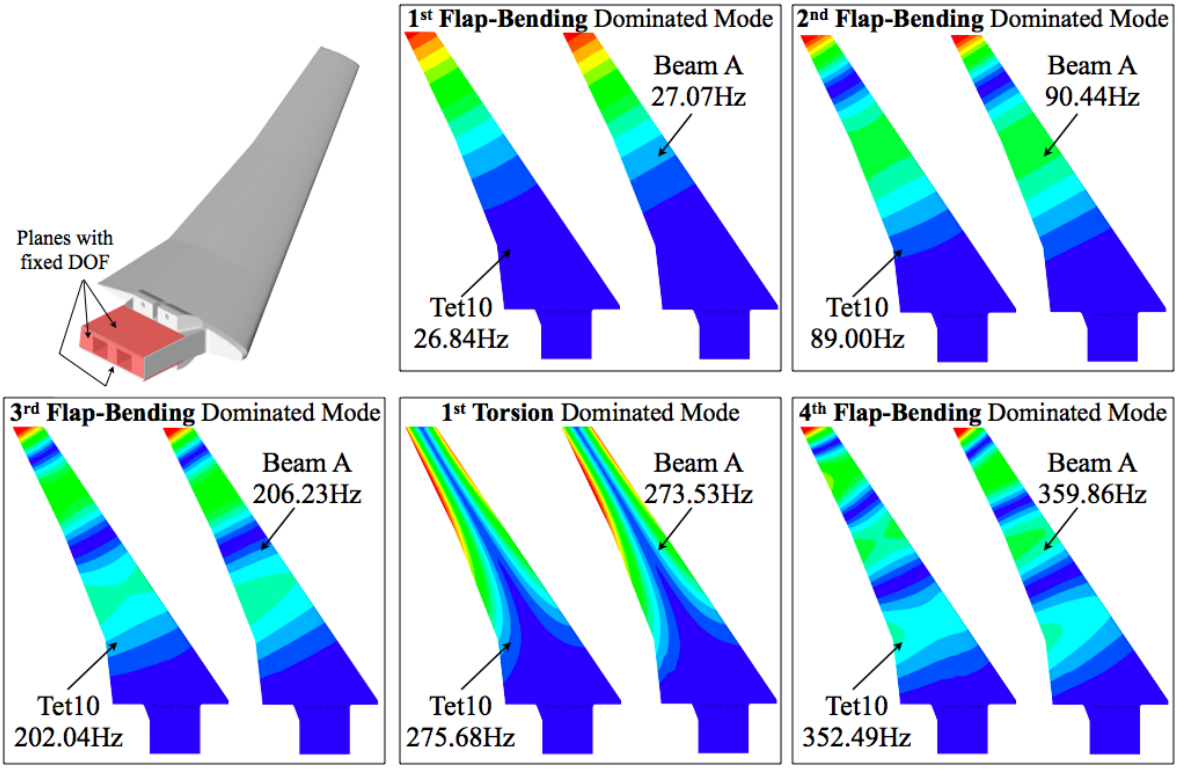

Figure 7: Comparison of mode shapes and vacuum eigenfrequencies of structural models with Tet10 volume and Timoshenko beam elements for the HIRENASD wing at T_{tot}=297K

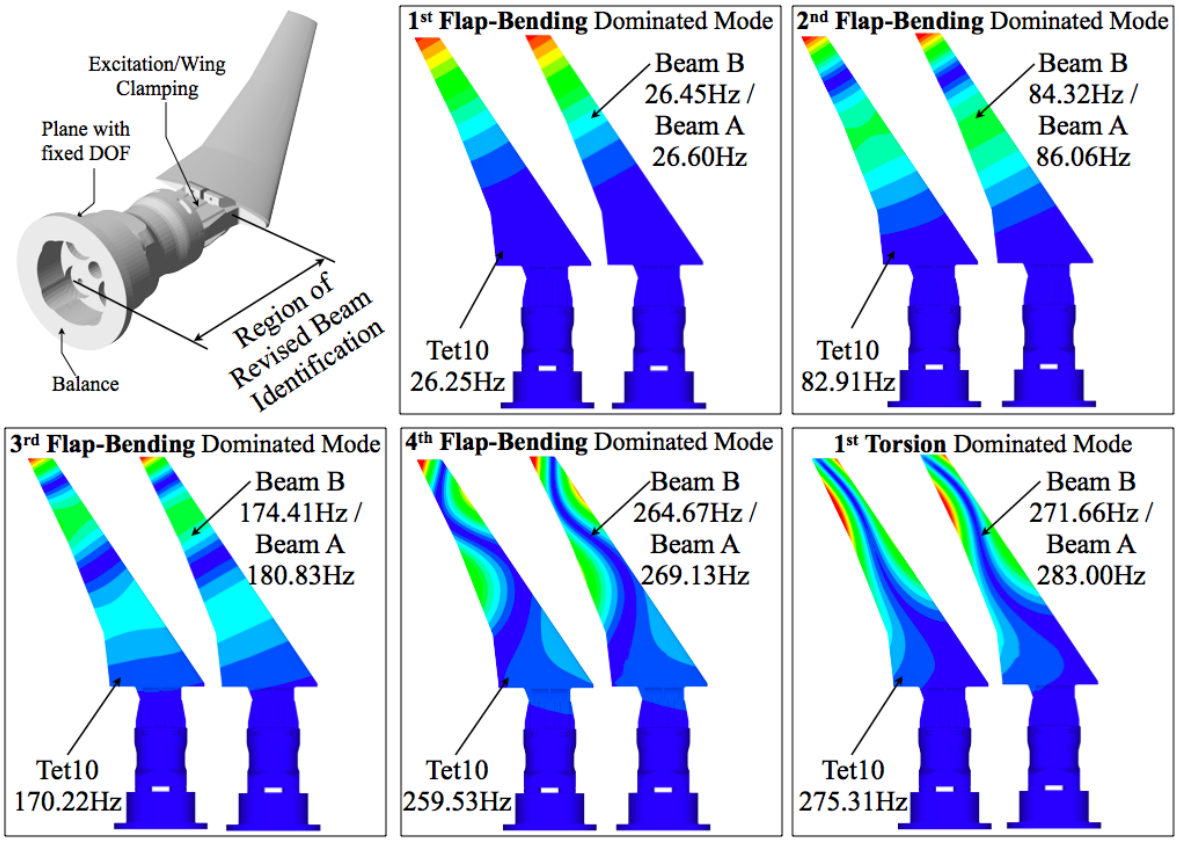

Figure 8: Comparison of mode shapes and vacuum eigenfrequencies of structural models with Tet10 volume and Timoshenko beam elements for the full HIRENASD model assembly consisting of wing, excitation mechanism and balance at T_{tot}=297K

resulting from these regions on eigenfrequencies could be captured accurately enough with the beam model by subjecting a proper volume model of the crucial parts to equilibrium load groups and deriving mean stiffnesses from model deformations. In doing so the highest relative deviation occurring for 3^{rd} flap-bending dominated mode could be reduced from over 6% to below 2.5%. Both the volume model and the beam model considering the excitation mechanism and the balance exhibit a strong coupling of mode shapes. The 4^{th} bending mode and the 1^{st} torsional mode have so prominent mode shape components in torsional resp. flap-bending direction that an assignment about which motion type dominates the mode can hardly be made. This is very different from the wing-only configuration (cf. Fig. 7).

Fig. 9 shows the structural mode shapes of the actual wind tunnel model which were evaluated by means of operational modal analysis from HIRENASD experiments under wind and with excitation turned on. The first through third mode shapes compare well to the numerical results given in Fig. 8. The 4^{th} flap-bending mode apparently still contains torsional deformation in the experiment, but the amount of flap-bending contribution is almost negligibly low for the torsion dominated mode identified in the experiment. This is entirely different in all numerical structural models prepared so far, regardless if these are volume or beam models.

The consideration of ETW's adapter between balance and model cart reduces the eigenfrequency of 4^{th} flap-bending mode by about 18Hz and separates this mode again from the torsion dominated mode (see Fig. 10). The latter remains more or less unchanged after adding the adapter to the model. The main influence originates from the increase of bending length and the local deformation occurring in the connection plane between upper balance part and adapter. A rest of torsional content still remains in the shape of the 4^{th} flap-bending mode, but this is in agreement with the behaviour of the wind tunnel model (cf. Fig. 9). The same eigenbehaviour as shown here based on a volume model (196000 Tet10 elements, 1.1m DoF) could be reproduced with a Timoshenko beam model with much fewer degrees of freedom (about 4000 DoF).

Overall the Timoshenko beam modelling is indeed capable of representing the flexibilities and inertias of all components of the HIRENASD assembly after revision of regions with non-smooth geometry changes. The ETW adapter which was not considered in previous modelling should be included in the numerical structural identification due to its separating effect of 4^{th} flap-bending and 1^{st} torsion mode and its improvement of eigenfrequencies towards the experimental ones.

6 NUMERICALLY PREDICTED AND OBSERVED AERO-STRUCTURAL MODEL DYNAMICS IN EXCITATION EXPERIMENTS

6.1 Influence of Model Excitation on Unsteady Pressure Distributions and Accelerations

In the course of the HIRENASD test campaign, experiments were conducted with wing excitation turned on under wind to measure the mutual influence between elastic harmonic wing oscillations in one of the mode shapes and transonic aerodynamics. In the same way it was done in the experiments (compare descriptions in [3, 6]), the vibration excitation was achieved in simulations by subjecting the Timoshenko beam model to an equilibrium

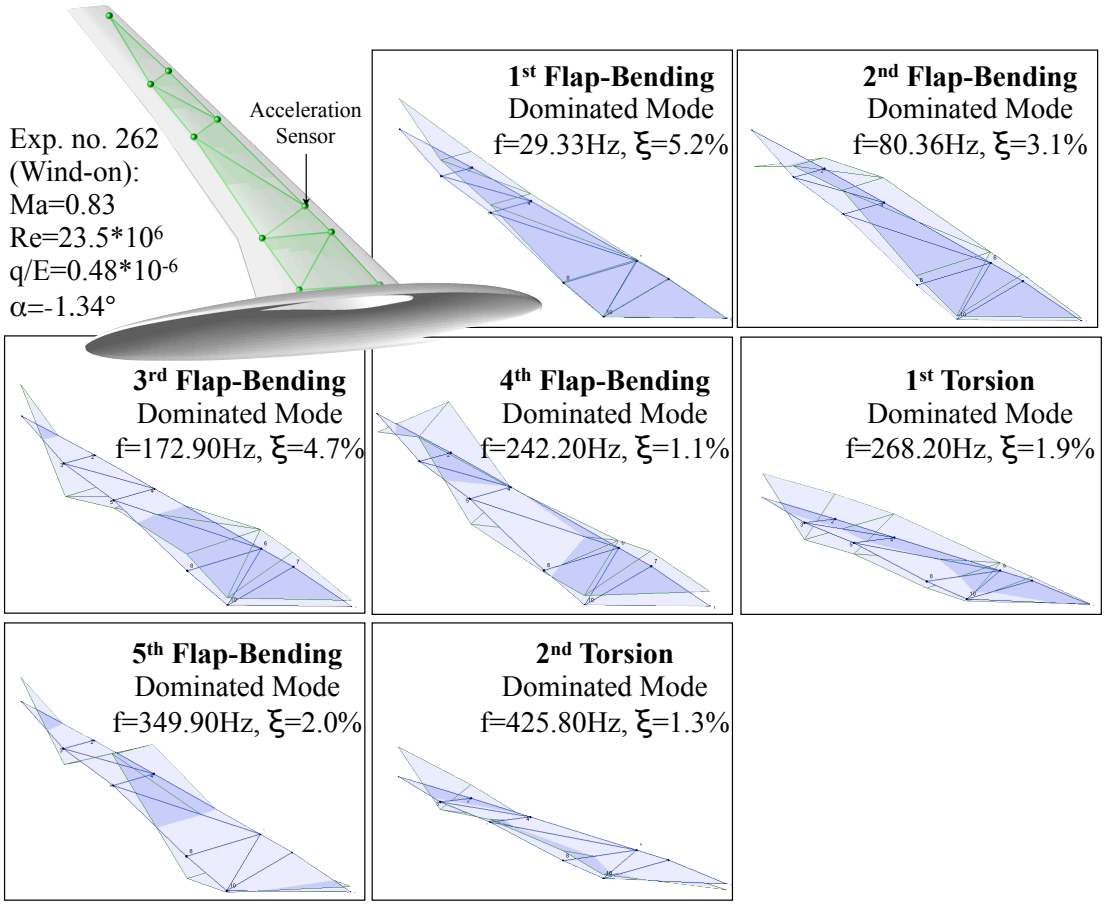

Figure 9: Eigenfrequencies, damping coefficients and mode shapes determined from a HIRENASD excitation experiment of series 5 at wind-on conditions (exp. 262: excitation of 1^{st} flap-bending dom. mode at Ma=0.83, Re=$23.5 \cdot 10^6$, q/E=$0.48 \cdot 10^{-6}$, T_{tot}=200.25K)

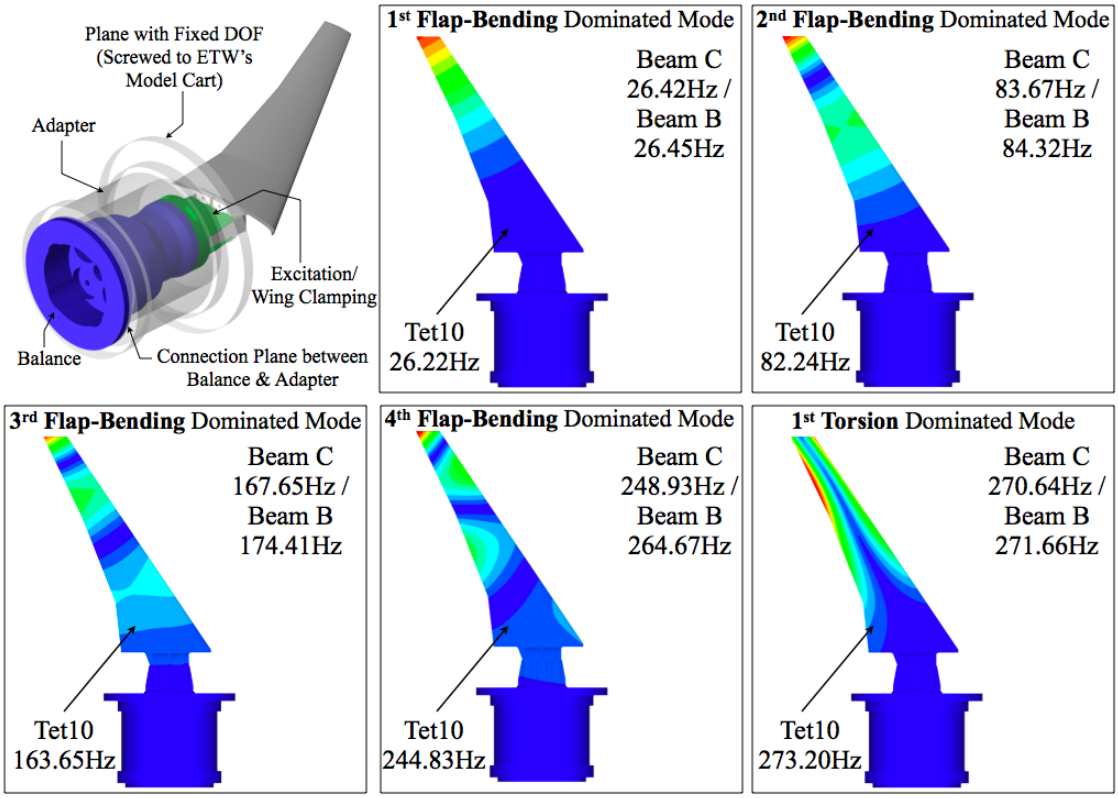

Figure 10: Mode shapes and vacuum eigenfrequencies of Tet10 volume element modelling for the full HIRENASD model assembly attached to ETW's model cart adapter at T_{tot}=297K

pair of time-harmonic bending moments at the wing root plane and at the end of the housing of the excitation piezos. Because the wing does not posses a symmetry plane, the excitation of a particular eigenmode can be performed by setting the oscillation frequency of the bending moments to the resonance frequency which was identified for the particular mode in a free vibration test under wind.

Subsequently, three dynamic experiments with excitation of different modes were simulated. The pressure fluctuations in the outermost wing section no. 7 as well as the acceleration patterns were compared with experimental data from a state with constant vibration amplitudes. To reduce disturbances contained in the measured raw signals, filtering techniques were applied as presented in [13] before comparing with the results from numerical simulations. The initial state, i.e. the AEC, is the same for all three experiments: The deformation state at wing tip is 4.2mm displacement, 0.28° twist and 0.16° torsional angle. Starting from this AEC the model was excited in its 1^{st} flap-bending (exp. 270), 2^{nd} flap-bending (exp. 271) and 1^{st} torsion mode (exp. 272). The subsequent results were achieved using beam model A. In the simulations, the oscillation amplitudes of the excitation moments were set according to the measurements of force couples in the experiments. The excitation frequencies were set according to the resonance frequency determined for the numerical aeroelastic model in free vibration tests conducted prior to excitation simulations [2]. Due to minor differences between the actual experimental aeroelastic system and the modelled one, there exist slight deviations in the excitation frequencies of experiment and simulation. The flow conditions, oscillation frequencies and amplitudes of the exciting equilibrium group of bending moments used in simulations are summarised in Tab. 1.

Mode	Ma	$\mathrm{Re}/10^6$	$\mathrm{q/E}/10^{-6}$	$\alpha/°$	f_{exc}/Hz	$\hat{M}_{exc}$/Nm	$T_{exc}/\Delta t$
1^{st} flap-bend.	|	|	|	|	29.50	1430	151
2^{nd} flap-bend.	0.80	23.5	0.48	$-1.34°$	87.37	1460	58
1^{st} torsion	|	|	|	|	270.50	1220	37

Table 1: Flow conditions, oscillation frequencies and amplitudes of the bending moment equilibrium group used for three different excitations of the numerical model

6.1.1 Excitation of 1^{st} Flap-Bending Dominated Mode

The wing was excited to vibrate harmonically in its 1^{st} flap-bending dominated mode by subjecting the structure to an equilibrium group of two bending moments. These oscillated according to the parameters given in the first row of Tab. 1. Constant vibrational amplitudes were reached after 0.5s of simulation time. The maximum flap-bending amplitude was 1.8mm at the wing tip, whereas the torsional angle amplitude was only 0.01°. The pressure fluctuations arising from this deformation are plotted in Fig. 11 over four excitation periods, separately for upper and lower side in the outermost wing section (section no. 7). The physical time was normalised with the respective excitation period of simulation and experiment because of slightly differing resonance frequencies between the both. The result of the simulation is depicted to the right in Fig. 11, the experimental result to the left. Although the numerical model was subjected to the amplitude of the excitation forces that was recorded in the experiments, deviations of wing accelerations emerged. To ease the comparison of achieved pressure fluctuations between experiment

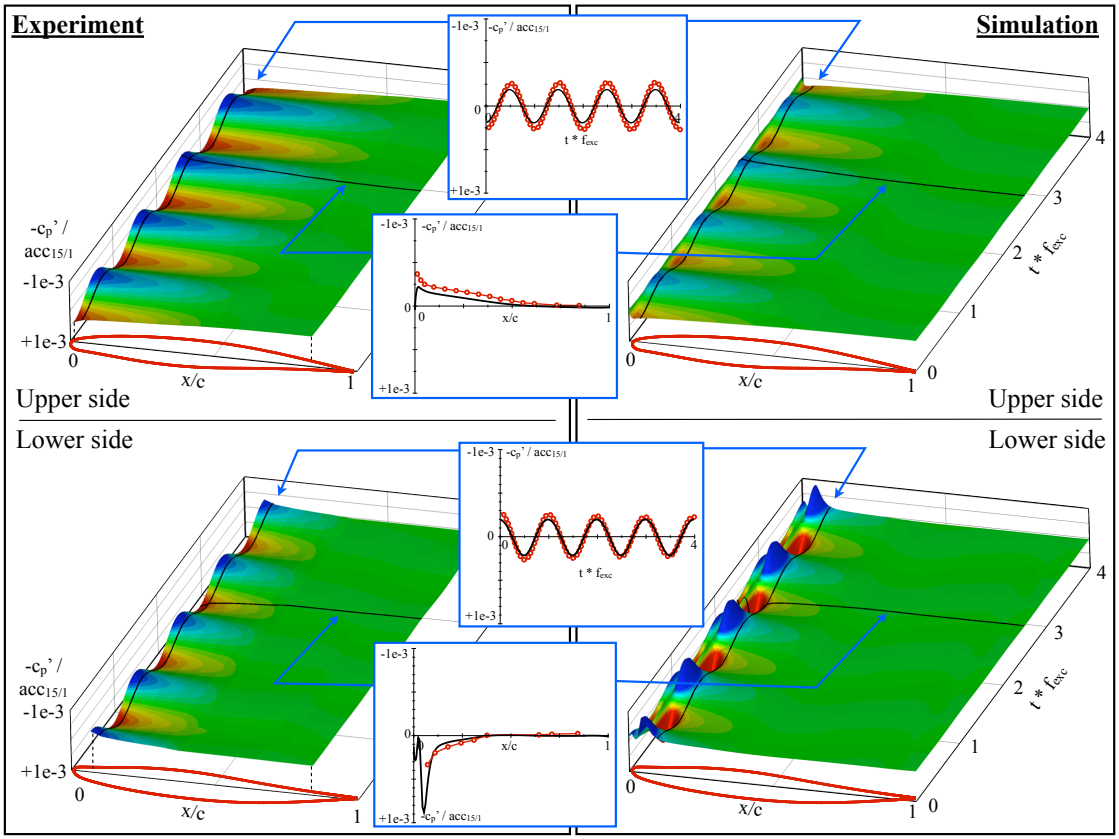

Figure 11: Unsteady pressure fluctuations normalised by mean amplitude of acceleration sensor 15/1 on upper and lower side of the outermost airfoil section due to excitation of 1^{st} flap-bending dom. mode (Ma=0.80, Re=$23.5 \cdot 10^6$, q/E=$0.48 \cdot 10^{-6}$, α=$-1.34°$, exp. 270, series 5)

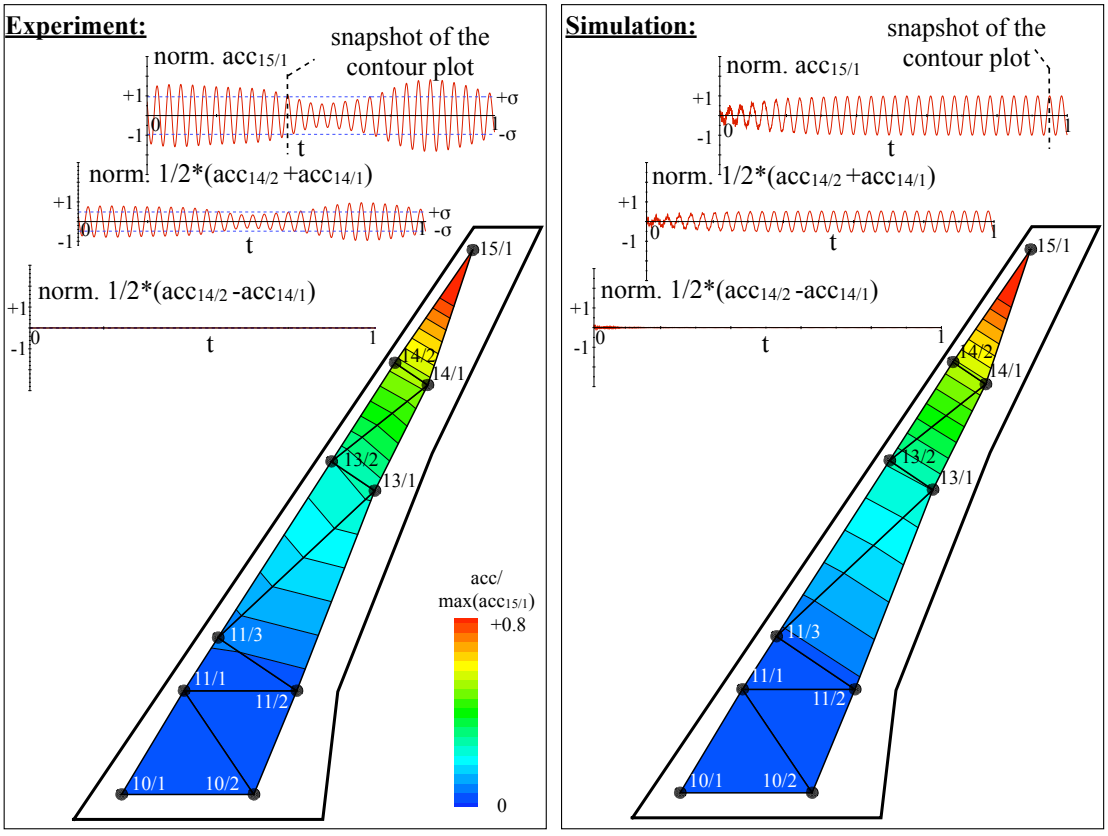

Figure 12: Normalised acceleration patterns of experiment and simulation resulting from excitation of 1^{st} flap-bending dom. mode during steady-state oscillation phase (exp. 270, series 5: Ma=0.80, Re=$23.5 \cdot 10^6$, q/E=$0.48 \cdot 10^{-6}$, α=$-1.34°$)

and simulation, the instantaneous pressure coefficient was normalised by the acceleration amplitude at the outermost sensor 15/1 (see Fig. 12) which was found in the simulation and experiment, respectively.

The numerically predicted normalised time dependent pressure field compares well with the experiment, even though latter exhibits marginally larger amplitudes. The influence on the pressure field in section no. 7 is most prominent in the leading edge region on the lower side of the wing. The inset diagrams depict the pressure history at 1% local chord and a snapshot of the chord-wise pressure distribution over the airfoil section.

Fig. 12 reveals that the model excitation lead to similar acceleration distributions in the experiment and simulation. The figure displays the acceleration distributions for two snapshots at which simulation and experiment reached one of their local maxima of acceleration. The maximum amplitude of acceleration occurring close to the wing tip (acc. sensor 15/1) was used to normalise the instantaneous acceleration. The good agreement of pressure fluctuation is due to the similarity of the acceleration distributions. Differences can only be recognised with regard to the isolines which are not oriented according to the beam theory in the innermost wing section but parallel to the incoming flow. The difference and sum of the time histories of accelerations at sensors 14/1 and 14/2 demonstrate that the wing motion is dominated more by flap-bending ($1/2(\mathrm{acc}_{14/2} + \mathrm{acc}_{14/1})$) than by torsion ($1/2(\mathrm{acc}_{14/2} - \mathrm{acc}_{14/1})$) in this wing section.

6.1.2 Excitation of 2^{nd} Flap-Bending Dominated Mode

The parameters of the second row of Tab. 1 were set to excite the 2^{nd} flap-bending dominated mode in the simulation. In this case the state of constant vibration amplitudes was reached after 0.6s due to a lower aerodynamic damping of the 2^{nd} mode than previously of the 1^{st} mode. For the same reason, the amplitude of the flap-bending deflection increased to 3.2mm, the torsional amplitude to 0.06°. The unsteady pressure fluctuation arising from this wing motion about the AEC and the corresponding acceleration distribution are plotted in Figs. 13 and 14.

With regard to the acceleration distribution the only difference which was observed between simulation and experiment again consisted in the differing orientation of the acceleration isolines in the inner wing section. But the basic shapes of motion were almost identical between numerical model and the experiment. Again the experiment shows a negligibly higher amplitude of pressure fluctuation. However, the development of fluctuations in time and their shape over the airfoil section are in very good agreement.

6.1.3 Excitation of 1^{st} Torsion Dominated Mode

As pointed out in section 5, the 1^{st} torsion-dominated mode of beam model A is actually more flap-bending dominated (cf. Fig. 8). It was excited by an equilibrium group of bending moments which oscillated according to the parameters of the third row of Tab. 1. The amplitude of the flap-bending deflection reaches 1.1mm, which is comparable to the value achieved by the excitation of the 1^{st} flap-bending dominated mode. The amplitude of torsional oscillation is significantly higher than in the previous two experiments at 0.51°. The acceleration distribution in Fig. 16 reveals that the excited mode shape of the numerical model has far higher components in flap-bending direction than the actual

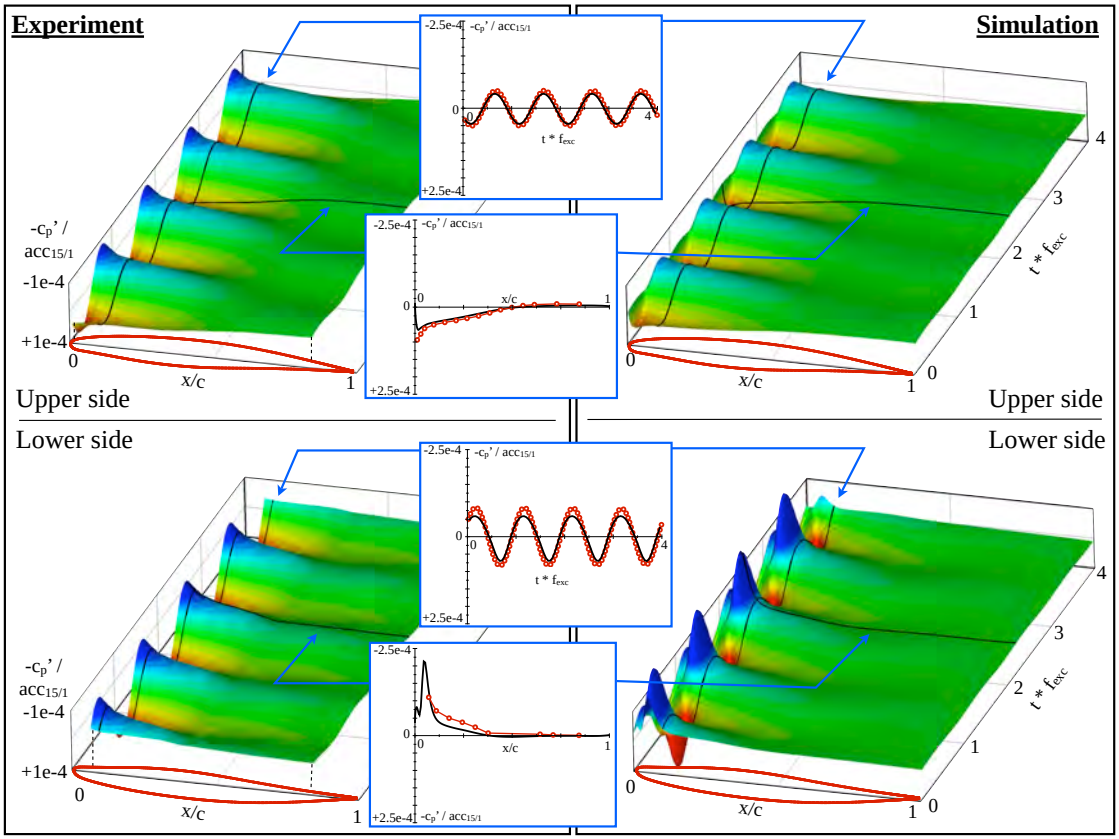

Figure 13: Unsteady pressure fluctuations normalised by mean amplitude of acceleration sensor 15/1 on upper and lower side of the outermost airfoil section due to excitation of 2^{nd} flap-bending dom. mode (Ma=0.80, Re=$23.5 \cdot 10^6$, q/E=$0.48 \cdot 10^{-6}$, α=$-1.34°$, exp. 271, series 5)

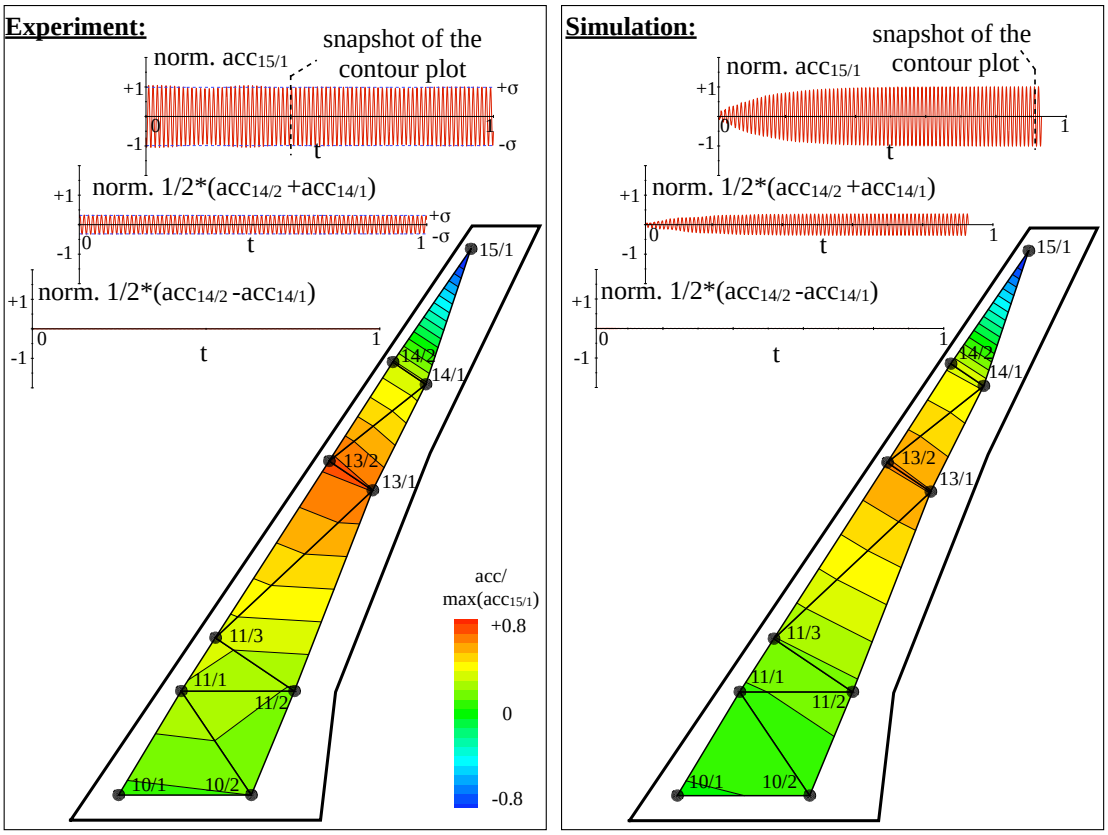

Figure 14: Normalised acceleration patterns resulting from excitation of 2^{nd} flap-bending dom. mode during steady-state oscillation phase (exp. 271, series 5: Ma=0.80, Re=$23.5 \cdot 10^6$, q/E=$0.48 \cdot 10^{-6}$, α=$-1.34°$)

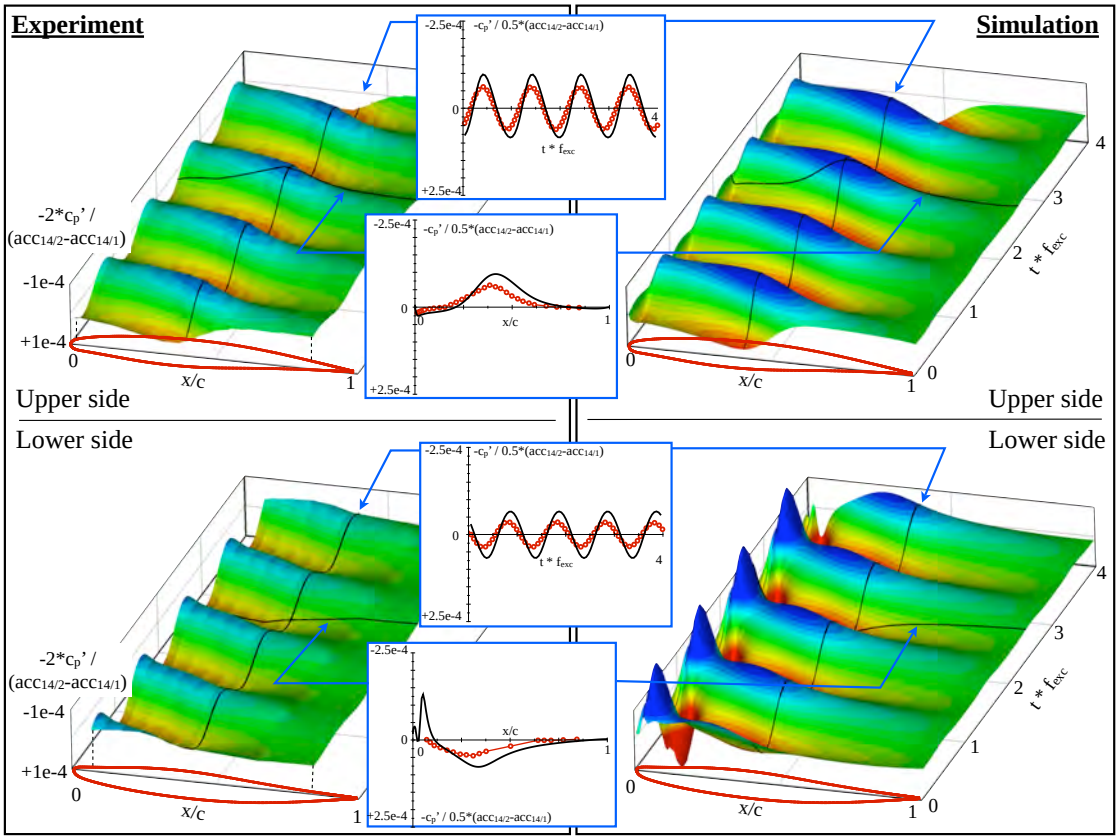

Figure 15: Unsteady pressure fluctuations normalised by mean amplitude of acceleration difference at sensors 14/2 and 14/1 on upper and lower side of the outermost airfoil section due to excitation of 1^{st} torsion dom. mode (Ma=0.80, Re=$23.5 \cdot 10^6$, q/E=$0.48 \cdot 10^{-6}$, α=$-1.34°$, exp. 272, series 5)

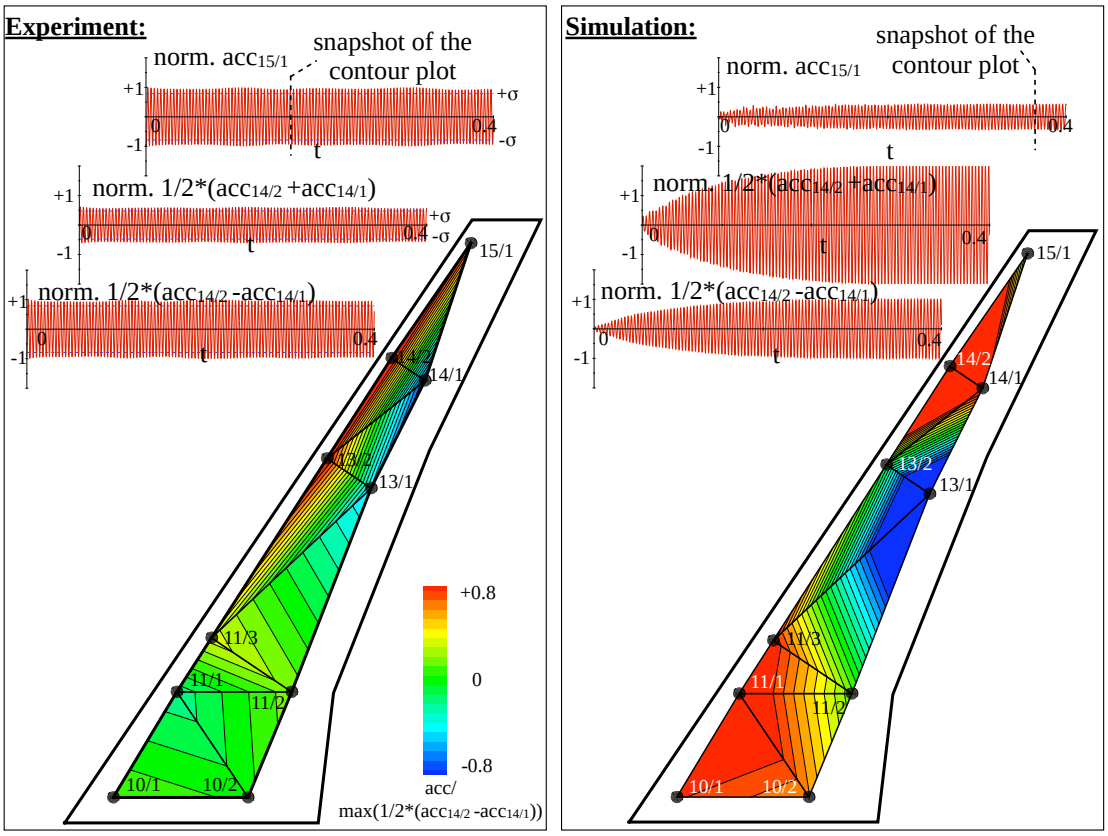

Figure 16: Normalised acceleration patterns resulting from excitation of 1^{st} torsion dom. mode during steady-state oscillation phase (exp. 272, series 5: Ma=0.80, Re=$23.5 \cdot 10^6$, q/E=$0.48 \cdot 10^{-6}$, α=$-1.34°$)

wind tunnel model. Because the pressure fluctuations shown in Fig. 15 are normalised by the acceleration, these appear only slightly higher in the experiment. In this case the accelerations at sensors 14/2 and 14/1 ($1/2(\mathrm{acc}_{14/2} - \mathrm{acc}_{14/1})$) were used instead of 15/1 as the values are more representative of the overall torsional motion. The pressure fluctuations associated with the torsional motion are primarily noticable around the centre of the chord. These are captured fairly well in the simulations. The additional motion of the numerical model in flap-bending direction shows in unsteady pressure peaks in the nose region on the lower side. These peaks were of course not detected in the experiments where the flap-bending motion was far less prominent. This result underlines the importance of also considering the flexibility of the adapter between ETW's model cart and the wind tunnel balance (cf. Figs. 8 and 10).

7 CONCLUSION AND OUTLOOK

In this paper comparisons of results from numerical simulations applying the CASD code SOFIA with selected static and dynamic HIRENASD wind tunnel experiments were presented. The dependence of lift on angle of attack, Mach number and loading factor were very accurately captured in static aeroelastic simulations employing SOFIA, even in the presence of strong shock-induced separations. In contrast, simulations disregarding the model deformation showed major differences in the inclination of the lift curve due to wrong shock positions and flow separation onsets. The Mach number at lift divergence onset was predicted correctly for all investigated angles of attack if the model deformation was considered. However, at very high Mach numbers ($\mathrm{Ma} \geq 0.85$) and angles of attack higher than 3.0°, with separation expected over the entire wing span, the agreement between computational predictions and the experiments worsened. Minor differences in pressure distributions were observed at very high Mach numbers in both innermost wing sections and in the vicinity of shock-induced separations which appeared to be stronger in the experiments than numerically predicted. This issue could neither be improved by employing a Reynolds stress model nor other eddy-viscosity-based turbulence models instead of the LEA two-equation turbulence model applied otherwise. Slight differences observed in the spanwise bending deflection of the model could not be attributed to the beam identification which produced almost identical deformation as the corresponding solid model, but might be attributed to the two-shell construction of the wind tunnel model which was not considered in the numerical model so far.

A revision of the structural model identification revealed that eigenshapes and eigenfrequencies are strongly influenced by the wind tunnel model support. The consideration of the adapter between ETW's model cart and the balance is essential to improve the agreement between computational and experimental eigenfrequencies, and in particular, to obtain a match between computational and experimental eigenshapes. Comparing experiments with excitation of 1^{st} and 2^{nd} flap-bending modes and their corresponding simulations, a very good agreement of the ratios of unsteady pressure amplitudes and excited accelerations can be stated. The use of the structural model without revision accounts for the slight discrepancy observed for the excitation of the torsional mode. The results obtained for selected excitations are very promising for evaluations and comparisons to be carried out next. These will focus on actual correlations between quantities representing the unsteady aerodynamic interaction in a more integral manner, e.g. the spanwise lift distribution, and the structural motion being excited. Further investigations will be made concerning the influences of Mach number and q/E on the ASD of the model.

8 REFERENCES

[1] Ballmann, J. (Ed.): *Flow Modulation and Fluid-Structure Interaction at Airplane Wings – Research Results of the Collaborative Research Centre SFB 401 at RWTH Aachen University.* Notes on Numerical Fluid Mechanics and Multidisciplinary Design, Vol. 84, Springer, 2003

[2] Reimer, L., Braun, C., Chen, B.-H., Ballmann, J.: *Computational Aeroelastic Analysis and Design of the HIRENASD Wind Tunnel Wing Model and Tests.* In proc. of the International Forum on Aeroelasticity and Structural Dynamics (IFASD) 2007, Paper IF-077, Stockholm, Sweden, 2007

[3] Korsch, H., Dafnis, A., Reimerdes, H.-G.: *Dynamic qualification of the HIRENASD elastic wing model*, Aerospace Science and Technology, Volume 13, Issue 2-3, 2009, pp. 130-138

[4] Ballmann, J., et al.: *Experimental Analysis of High Reynolds Number Aero-Structural Dynamics in ETW.* In proc. of the 46^{th} AIAA Aerospace Sciences Meeting and Exhibit, Paper AIAA-2008-841, Reno, Nevada, United States of America, 2008

[5] Ballmann, J., et al.: *The HIRENASD project: High Reynolds number aero-structural dynamics experiments in the European Transonic Windtunnel (ETW).* In proc. of the International Congress of the Aeronautical Sciences 2006, Paper ICAS 2006-5.11.2, Hamburg, Germany

[6] Dafnis, A., Korsch, H., Buxel, C., Reimerdes, H.-G.: *Dynamic Response of the HIRENASD Elastic Wing Model under Wind-Off and Wind-On conditions.* In proc. of the International Forum on Aeroelasticity and Structural Dynamics (IFASD) 2007, Paper IF-073, Stockholm, Sweden, 2007

[7] Braun, C.: *Ein modulares Verfahren für die numerische aeroelastische Analyse von Luftfahrzeugen.* Doctoral thesis, RWTH Aachen University, 2007

[8] Beckert, A.: *Coupling fluid (CFD) and structural (FE) models using finite interpolation elements.* Aerospace Science and Technology, Volume 4, Issue 1, 2009, pp. 13-22

[9] Reimer, L., Wellmer, G., Braun, C., Ballmann, J.: *Computational Methods for Aero-Structural Analysis and Optimisation of Aircrafts based on Reduced-Order Structural Models.* Kroll, N. Schwamborn, D., Becker, K., Rieger, H., Thiele, F. (Eds.): *MEGADESIGN and MegaOpt – Aerodynamic Simulation and Optimization in Aircraft Design.* In Notes on Numerical Fluid Mechanics and Multidisciplinary Design, Springer, 2008

[10] Boucke, A.: *Kopplungswerkzeuge für aeroelastische Simulationen.* Doctoral thesis, RWTH Aachen University, 2003

[11] Kroll, N., Faßbender, J. K. (Eds.): *MEGAFLOW – Numerical Flow Simulation for Aircraft Design.* Notes on Numerical Fluid Mechanics and Multidisciplinary Design, Vol. 89, Springer, 2005

[12] Hesse, M.: *Entwicklung eines automatischen Gitterdeformationsalgorithmus zur Strömungsberechnung um komplexe Konfigurationen auf Hexaeder-Netzen.* Doctoral thesis, RWTH Aachen University, 2006

[13] Ballmann, J., Boucke, A., Reimer, L., Dickopp, C.: *Results of Dynamic Experiments in the HIRENASD Project and Analysis of Observed Unsteady Processes.* In proc. of the International Forum on Aeroelasticity and Structural Dynamics (IFASD) 2009, Paper IFASD-2009-103, Seattle, Washington, United States of America, 2009